Materials & Design 213 (2022) 110303

Contents lists available at ScienceDirect

Materials & Design

journal homepage: www.elsevier.com/locate/matdes

Core-shell Fe@Fe_xO_y nanoring system: A versatile platform for biomedical applications

Bianca M. Galeano-Villar [a], Richard J. Caraballo-Vivas [a], Evelyn C.S. Santos [a], Raimundo C. Rabelo-Neto [b], Sara Gemini-Piperni [c,f], Priscilla V. Finotelli [d], Noemi R. Checca [a], Carlos S.B. Dias [e], Flávio Garcia [a,*]

[a] Brazilian Center for Research in Physics, Zip Code 22290-180 Urca, Rio de Janeiro, Brazil
[b] National Institute of Technology, Zip Code 20081-312, Rio de Janeiro, Brazil
[c] Unigranrio University, Zip Code 25071-202, Duque de Caxias, Rio de Janeiro, Brazil
[d] Federal University of Rio de Janeiro, Faculty of Pharmacy, University City, Zip Code 21941-170, Rio de Janeiro, Brazil
[e] Brazilian Center for Research in Energy and Materials (CNPEM), Brazilian Synchrotron Light Laboratory (LNLS), Zip Code 13083-970 Campinas, Sao Paulo, Brazil
[f] Federal University of Rio de Janeiro, Institute of Biomedical Sciences, Zip Code 21941-902 Rio de Janeiro, Brazil

HIGHLIGHTS

- Two-step preparation of a core@shell (Fe@Fe_xO_y) nanotube system allows the tunning of the metallic iron and iron oxide phases.
- The Fe@Fe_xO_y nanotubeś magnetic saturation can adjust for a desirable application by varying the synthesis conditions.
- The Fe@Fe_xO_y nanotubes have a vortex state, which guarantees low remanence and coercivity.
- Fe@Fe_xO_y nanotubes present good biocompatibility for two cells line: HEK and SAOS2.

GRAPHICAL ABSTRACT

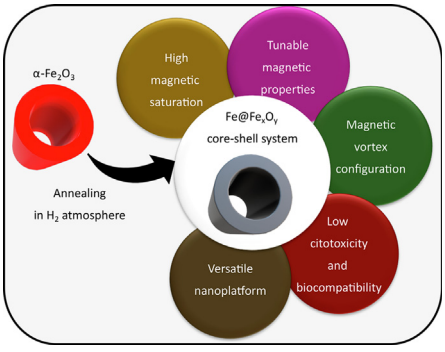

ARTICLE INFO

Article history:
Received 19 June 2021
Revised 22 September 2021
Accepted 4 December 2021
Available online 7 December 2021

Keywords:
Core–shell
Nanoring
Vortex
Biocompatibility
Metallic iron
Iron oxides

ABSTRACT

Iron oxide (maghemite and magnetite) nanoparticles are the most commonly used magnetic materials in nanomedicine because of their high biocompatibility. However, their low saturation magnetization (60–90 emu/g) limits their applicability. Here, we report a new core–shell (Fe@Fe_xO_y) nanoring system, which combines the high magnetic saturation of a metallic iron core (220 emu/g) and the biocompatibility of an iron oxide shell. To produce these nanostructures, hematite (α-Fe_2O_3) nanorings were annealed in a H_2 gas atmosphere for different periods to optimize the amount of metallic iron percentage (δ) in the system. Thus, nanostructures with different magnetic saturation (97 to 178 emu/g) could be obtained; based on their metallic iron content, these particles are labeled as Vortex Iron oxide Particle δ (VIPδ). Micromagnetic simulations confirmed that the VIPδ nanorings exhibit a vortex configuration, guaranteeing low remanence and coercitivity. Moreover, the system shows good biocompatibility in various assays as determined through cell viability measurements performed using two different human cell lines, which were exposed to VIP78% for 24 h. Therefore, VIPδ nanorings combine a magnetic vortex state and biocompatibility with their high magnetic saturation and can thus serve as a platform that can be tuned during the synthesis based on desired biomedical application.

* Corresponding author at: Brazilian Center for Research in Physics, Zip Code 22290-180 Urca, Rio de Janeiro, Brazil.
E-mail address: flavio.cbpf@gmail.com (F. Garcia).

https://doi.org/10.1016/j.matdes.2021.110303
0264-1275/

1. Introduction

Magnetic Iron Oxide Nanoparticles (MIONs) have attracted much attention, especially for use in various biomedical applications such as magnetic resonance imaging (MRI) [1,2], stimuli-responsive drug delivery [3–6], bioseparation [7,8], and magnetic hyperthermia (MH) [9–12]. Recently, interest in theranostic systems (*i.e.*, those combining both therapy and diagnostics) for cancer prevention has also increased significantly. Thus, improving the magnetic properties of MIONs would allow for earlier detection of cancer and more efficient treatments. For these reasons, Superparamagnetic Iron Oxides Nanoparticles (SPIONs), a class of MIONs, are today's more explored to use as theranostic agents because of their biocompatibility, low cytotoxicity, zero remanence, and coercivity, which meet the requirement for various biomedical applications [13–15]. SPIONs such as magnetite (Fe_3O_4) and maghemite (γ-Fe_2O_3) nanospheres have been approved for a number of *in-vivo* applications by the Food and Drug Administration (FDA), and their suspensions are commercially available [16]. However, the saturation magnetizations of Fe_3O_4 and γ-Fe_2O_3 are relatively low (60–90 emu/g) compared with those of conventional ferromagnetic materials such as metallic Fe (220 emu/g) [17], limiting the use of the nano compounds based on these oxides as theranostic agents.

The design and tuning of the composition, size, and shape of magnetic theranostic agents can be improved. One way to enhance the magnetic properties of these materials is to partially replace the iron ions those of other 3d metals, which are also called spinel ferrites (MFe_2O_4, where M = Co, Mn, Ni) [18,19]. However, the cytotoxicity of nano ferrite compounds is not yet known. Additionaly, magnetic core–shell systems have been shown to exhibit improved magnetic properties [17,20]. Another option is to form a core composed of high magnetic moment material, such as metallic iron, and surround it with a biocompatible shell made of Fe_3O_4 or γ-Fe_2O_3 [20]. Thus, in this configuration, the metallic core is enveloped by a biocompatible shell, which prevents its oxidation and helps ensure a higher degree of magnetization saturation. The shell also allows for surface functionalization [11,21].

Another strategy to modify the magnetic properties of nanocompounds is to vary the morphology, that is, to form compounds structured as nanocubes [22,23], nanowires/nanorods [24,25], nanoflowers [26,27], and octopods [28]. Studies have demonstrated that morphological tuning allows to control of the magnetic properties [22,23,29,30] of these materials. Recently, Mohapatra *et al.*[29] showed that, by tuning the morphology of iron oxide nanoparticles (*i.e.*, by forming spheres, cubes, octahedrons, multipods, nanowires, and nanorods), the heating efficiency of high-aspect-ratio nanowire-shaped iron oxide nanoparticles for magnetic heating applications could be improved significantly compared with that of spherical nanoparticles. This was owing to the high shape anisotropy of the former. Sharma *et al.* [23] synthesized cubic magnetite that simultaneously exhibited superparamagnetic and paramagnetic behaviors by controlling the shape and size of the nanoparticles. The resulting material was suitable for use as a dual-modal MRI contrast agent. Thus, the morphology has a determining effect on the magnetic properties at the nanoscale, and morphological tuning may allow for novel magnetization configurations, such as vortex-domains observed in nanodiscs/-nanorings/nanotube [31–37]. This strategy can be exploited to develop new theranostic agents as alternatives to conventional spherical SPIONs.

Within this context, Vortex Iron oxide Particles (VIPs) exhibit an exotic magnetic configuration, which is denominated as a vortex ground state. In this configuration, the magnetic moments are oriented coplanar and tangentially to a static circular [38]. It is crucial to point out that nanoparticles with a vortex state show negligible coercivity and remanence, resulting in enhanced colloidal stability owing to the waker dipole–dipole interactions between particles in suspensions forms [35]. The dimensions of the particles, such as height and inner and outer diameters, can be accurately designed to promote the formation of a stable vortex domain [39]. The most common synthetic route for forming VIPs is the post-synthesis annealing process in the presence of a reducing gas [31,33,34,40–43]; however, the precise control synthesis and tuning processes for these materials remains a challenge. We had previously reported that Fe_3O_4 VIPs with superior shape-induced vortex magnetic properties and size tunability (70–250 nm in height) exhibit a significantly enhanced Specific Absorption Rate (SAR) and hence greater magnetic heating capability compared with those of SPIONs [31]. Fan *et al.*[44] reported nanorings that have a powerful effect on the T2*-weighted MRI signal compared with conventional SPIONs.

These results are attributable to the ring-like shape of these materials and their magnetization configuration, which ranges from vortex-like to onion-like and leads to a high relative volume fraction and susceptibility. Thus, VIPs are an exciting alternative to SPIONs but exhibit more exotic magnetic properties [31,45].

Herein, we describe the synthesis of core–shell iron@iron oxide VIPs and their structural, morphological, and magnetic properties, which make them suitable for use as a tunable theranostic nanoplatform. Hematite (α-Fe_2O_3) nanorings with an aspect ratio of approximately one were synthesized by a hydrothermal method [31,32]. The as-prepared α-Fe_2O_3 nanorings were then annealed in an H_2 atmosphere for different periods (30–240 min) to produce a core–shell ($Fe@Fe_xO_y$) structure with different Fe contents (δ). The VIPδ samples were characterized by *ex-situ* X-ray diffraction (XRD) analysis, field emission scanning electron microscopy (FESEM), X-ray photoelectron spectroscopy (XPS), and magnetic measurements. *In-situ* XRD and X-ray absorption near-edge spectroscopy (XANES) were performed during the reduction step using a synchrotron light source. Micromagnetic simulations confirmed the presence of a vortex state in the VIPδ nanorings. In addition, 3-(4 ,5-dimethylthiazol-2-yl)-2,5-diphenyltetrazolium bromide (MTT) and live/dead were performed with epithelial cells from human kidney embryos (HEK293) and human osteosarcoma cells lines (SAOS2) using 20–500 μg/mL of VIPδ. It is crucial to highlight that the tuning of the nanoring-shaped $Fe@Fe_xO_y$ core–shell structure did not result in cytotoxicity. Thus, this novel versatile theranostic nanoplatform shows interesting magnetic properties for biological applications, including drug delivery, magnetic hyperthermia, magnetic separation, and magnetic resonance imaging.

2. Experimental section

2.1. Chemicals

Iron (III) chloride hexahydrate ($FeCl_3.6H_2O$) and sodium sulfate (Na_2SO_4) were purchased from Vetec. Sodium phosphate monobasic ($NaH_2PO_4.H_2O$) was purchased from Química Moderna. All the chemicals were used as received. The mixture gas 10% H_2/Ar (*i.e.*, 10% of hydrogen and 90% of argon) used in the experiment was supplied by Messer.

2.2. Synthesis of hematite nanoring

Hematite ($\alpha - Fe_2O_3$) nanorings were synthesized as described in the literature, with minor modifications [32]. $FeCl_3.6H_2O$ (5.410 g, 20 mmol), Na_2SO_4 (0.041 g, 0.30 mmol) and

$NaH_2PO_4.H_2O$ (0.75 g, 0.55 mmol) salts were dissolved in 1000 mL of distilled water under vigorous stirring, resulting in a solution with a concentration of 20.00, 0.55 and 0.30 mmol/L, respectively. After the complete dissolution of the salts, 80 mL of the resulting solution was transferred to a Teflon cup, which was placed in a stainless-steel autoclave, and heated at 220 °C for 48 h at a rate of 20 °C/min. The solid was centrifuged, washed with isopropanol four times, and dried at 60 °C for 12 h to obtain a red powder (100 mg).

2.3. Ex-situ preparation of the vortex iron particles (VIPδ)

To produce magnetite/maghemite ($Fe_3O_4/\gamma - Fe_2O_3$) nanorings with different percentages of metallic iron (Fe), the synthesized $\alpha - Fe_2O_3$ nanorings were reduced in the presence of a continuous flow (70 mL/min) of 10 % H_2/Ar at different temperatures (300 °C to 400 °C) and fixed time of 120 min; and at a fixed temperature of 400 °C during different times (30 to 240 min). The amount of metallic iron in the samples was tailored by varying the reduction time from 30 to 240 min. After this annealing, the nanoparticle was cooled to room temperature and manipulated in air.

2.4. Characterization

The *ex-situ* X-ray diffraction (XRD) measurements were performed for 2θ of 20°–80°, using a X'pert PRO Panalytical diffractometer equipped with a XCelerator detector and a Cu–Kα (λ = 1.54056 Å) radiation source. The diffractograms were adjusted by the Rietveld method with the software FullProf [46], using the $\alpha - Fe_2O_3$ (R3c space group), Fe_3O_4 (F d3m space group) [47], FeO (F m3m space group) [47] and Fe (Im3m space group) [48] models.

The magnetic measurements (M × H) were performed using a Vibrating Sample Magnetometer (VSM) (Dynacool, Quantum3Design) at room temperature.

The morphologies of the samples were investigated using Field Emission Scanning Electron Microscopy (FESEM). The images were acquired on a field emission JEOL 7100FT instrument operated at 10 kV; the working distance was 10 mm, equipped with a backscattered detector, available at LABNANO/CBPF. Before the analysis, the samples were dispersed in ethanol and sonicated for 10 min. Then, the dispersion was gently dropped onto a Si substrate and left to dry at 60 °C for 24 h. The particle size distribution was determined from SEM images by measuring the height (H), internal diameter (d), and external diameter (D) of at least 200 particles using the software ImageJ.

The X-ray Photoelectron Spectroscopy (XPS) measurements were carried out using a SPECS PHOIBOS 100/150 spectrometer with a polychromatic Al-Kα radiation source at an X-ray energy of 1486.6 eV. The take-off angle for the C1s, O1s, and Fe2p energy peaks were 30°. The peaks were fitted using the software CASA-XPS; the calibration was performed using the C1s peak with a binding energy of 284.6 eV. The Fe 2p envelopes peaks were fitted using a proposed model [49], wherein the area of the higher energy peak, corresponding to $Fe2p_{1/2}$, was half that of the $Fe2p_{3/2}$ peak, and the energy difference between them was 13.6 eV [13].

In-situ X-ray Absorption Near Edge Spectroscopy (XANES) measurements were performed at the DXAS beamline at the Brazilian Synchrotron Light Laboratory (LNLS) [50], Campinas, Brazil. The XANES spectra were collected at the Fe–K edge (from 7035 to 7300 eV) in the transmission mode. For these measurements, 5 mg of hematite nanoring was mixed with 95 mg of boron nitride (BN) to prepare a pastille and adjust for optimum X-ray transmission. Then, *in-situ* reduction was performed with a flow of (70 mL/min) of hydrogen/helium (5% H_2/He) for maximum X-ray transmission. The initial temperature was 22 °C, the system was heated to 400 °C at a rate of 13 °C/min, and the temperature was then kept constant for 360 min. Subsequently, the system was cooled to the initial temperature at the same rate. During the experiment, 264 spectra were collected at one-minute interval. The *ex-situ* spectra of the reference samples were also collected. The spectra obtained during the *in-situ* experiments were analyzed by the software Athena, based on a linear combination of the reference spectra.

In-situ X-ray powder diffraction (XRD) measurements were carried out at the beamline XRD1-D12A [51] of LNLS. The sample was loaded into a quartz capillary with a diameter of 1.0 mm and placed between two quartz wool beds. The capillary was then placed in a reaction cell oriented horizontally and perpendicularly to the X-ray beam and connected to a 3-circle Heavy Duty diffractometer from Newport®. A hot air blower was coupled to a robotic arm (Yaskawa-Motoman) to hold the sample to control the temperature during the experiment. The diffractograms were recorded while the sample was reduced in a maximum He concentration at the maximum capillary flow possible of 10% H_2/He (10 mL/min) while increasing the temperature from 25 to 400 °C at rate of 10 °C/min. Subsequently, the sample was kept at this temperature for 120 min. The diffraction patterns were obtained in the 2θ range of 10–120° for an acquisition time of 120 s using an array of 24 detector Mythen (Dectris®), which were installed in the delta circle at 760 mm from the sample. The wavelength used (λ = 1.0332 Å) was selected by a double-crystal Si (1 1 1) monochromator and calibrated using an Al_2O_3 (SRM 676a) powder NIST standard.

2.5. Micromagnetic simulations

The micromagnetic simulations were performed using the Mumax 3.9 package, which allows one to analyze the time evolution of the magnetization distribution by solving the Landau-Lifshitz-Gilbert-Langevin equation. The experimentally accepted magnetic parameters for bulk Fe_3O_4 for the shell while those for metallic Fe for the core were used. More specifically, the saturation of magnetization (M_s was taken to be 220 emu/g for Fe and 90 emu/g for Fe_3O_4), the exchange stiffness (A was taken to be $10e^{-3}$), and the anisotropy (K) for both magnetite and iron were taken to be cubic. In addition, a cube with a size of 2 nm was used, and the Gilbert damping coefficient was set to α = 0.5.

2.6. Cytotoxicity assays

Human Osteosarcoma (SAOS2) and Human Embryonic Kidney 293 (HEK) cell lines were seeded at 50000/cm^2 for 24 h in Dulbecco Modified Eagle's Minimal Essential medium (DMEM), supplemented with 10% Fetal Bovine Serum (FBS) and 1% Penicillin Streptomycin (PS) at 37 °C in a controlled 5% CO_2 atmosphere. After adhesion, the cells were exposed to 20, 50, 70, 100, and 500 μg/mL of VIP78% for 24 h. The positive control used was 1% Sodium Dodecyl Sulfate (SDS). After exposure, the MTT (Sigma, Co. M2128) assay was performed according to the manufacturer's instructions. The cell viability is expressed in terms of percentage versus the control. The results are presented as the mean ± standard deviation of the values from three experiments ($^*p < 0.005$).

Live/Dead Viability/Cytotoxicity Kit for mammalian cells (Thermo Fisher Scientific, L3224) assays were performed after exposure to 100 μg/mL VIP78% for 24 h, as per the manufacturer's instructions. The positive control was exposed to 20% DMSO for 30 min before staining. Photomicrographs were taken during the experiments using a ZEISS AXIO A1 fluorescence microscope, and all experiments were performed thrice.

3. Results and discusions

3.1. Hematite nanorings

The hematite nanorings were synthesized using the method reported previously by Jia *et al.* [32]. XRD measurements were carried out to confirm the crystallographic structure of the nanoparticles; the data were adjusted using the Rietveld method. Fig. S1 (a) shows that all the peaks correspond to the corundum structure of hematite [47] without additional phases. The morphology of the particles was examined by FESEM; Fig. S1 (b) shows that they had a ring-like morphology. The size distribution of the nanorings is shown in Fig. S2. The histograms were adjusted using a Gaussian, the mean values of the height and internal and external diameters were: ⟨H⟩ = (175 ± 21) nm, ⟨d⟩ = (92 ± 16) nm, and ⟨D⟩ = (171 ± 15) nm, respectively. The dimensions were chosen to ensure an aspect ratio (*i.e.*, height/ external diameter) close to 1 to prevent the adverse effects of a high degree of asymmetry in the morphology [31,32].

3.2. VIPδ nanorings

The synthesized hematite nanorings were reduced to iron-magnetite/maghemite. For this, the red powder was annealed 10% H_2/Ar at different temperatures for 120 min. Fig. S3 (a) shows the conventional XRD data of the samples after the reduction process for temperatures from 300 °C to 400 °C. The XRD pattern of hematite is also plotted for comparison, a room temperature indicates it. Fig. S3 (b) shows the phases quantification from the Rietveld refinement for magnetite (blue curve)/maghemite (cyan curve), metallic iron (red), and hematite (blue); note that the metallic iron percentage increases as the temperature increase, and the maximum value obtained was 70% at 400 °C. In order to investigate the formation of the metallic iron as function of the annealing time, the temperature was fixed at 400 °C, and the time varied from 30 to 240 min. Fig. 1 (a) shows the conventional XRD data of the samples, the annealing time is indicated in each diffractogram. The diffractogram of hematite is denoted by a reduction time of zero. The phases contents (percentage) as determined from the Rietveld refinement are shown as functions of the annealing time in Fig. 1(b). As can be seen from Fig. 1 (a) and (b), annealing time of 30 min was necessary to reduce the hematite phase (black curve) to magnetite (blue curve)/maghemite (cyan curve) and wustite (magenta curve). It is important to highlight the fact that because the lattice parameters of maghemite and magnetite are similar [52,53], the XRD measurement could not distinguish between these phases; therefore, these phase contents are shown in same curve using the blue cyan rhombuses and blue squares, respectively. With an increase in the annealing time, the magnetite/maghemite was reduced to metallic iron (red curve), with 43% maghemite/magnetite and 49% metallic iron forming after 90 min. The maximum metallic iron content was 78%, which was obtained after 180 min. This value remained unchanged with further increases in the annealing time. In all the cases, the fraction of wustite phase remained almost constant at approximately 10%. This was unexpected as it is well known that stoichiometric wustite is unstable at room temperature [54]. Unsurprisingly, the unit cell volume of every phase, namely, magnetite/maghemite, wustite, and metallic iron, remained constant for all the reduction conditions and corresponded to the different metallic iron contents on the nanorings, as shown in Fig. 1 (c). Henceforth, the as-prepared samples are labeled as VIPδ, where δ indicates the iron content (%) on the nanorings. The morphology of the nanoparticles and their size distribution (D, d, and H) before and after the reduction process were investigated by FESEM. A representative image of the hematite nanoparticles is presented in Fig. 2 (a) while the

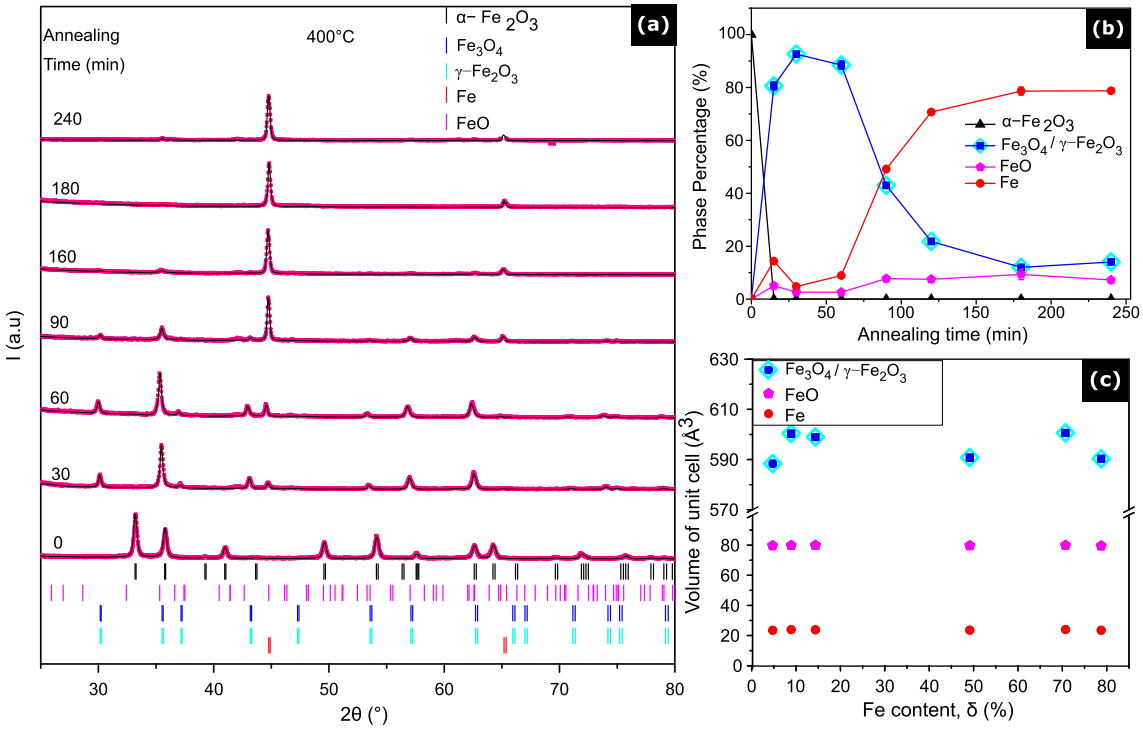

Fig. 1. (a) XRD diffraction patterns of as-prepared samples. Black lines represent the calculated adjustment by Rietveld analysis from FullProf software; vertical lines correspond to crystallographic plane reflections of hematite (black), magnetite (blue), maghemite (cyan) wustite (magenta), and metallic iron (red). (b) Phases percentage as functions of annealing time; magnetite and maghemite are shown together in same curve as the XRD technique can not distinguish between these phases. Note that metallic iron content increases with time; (c) Volumes of unit cells of all phases as functions of metallic iron content. For (b) and (c) error bars are on order of graph point symbol size. (For interpretation of the references to color in this figure legend, the reader is referred to the web version of this article.)

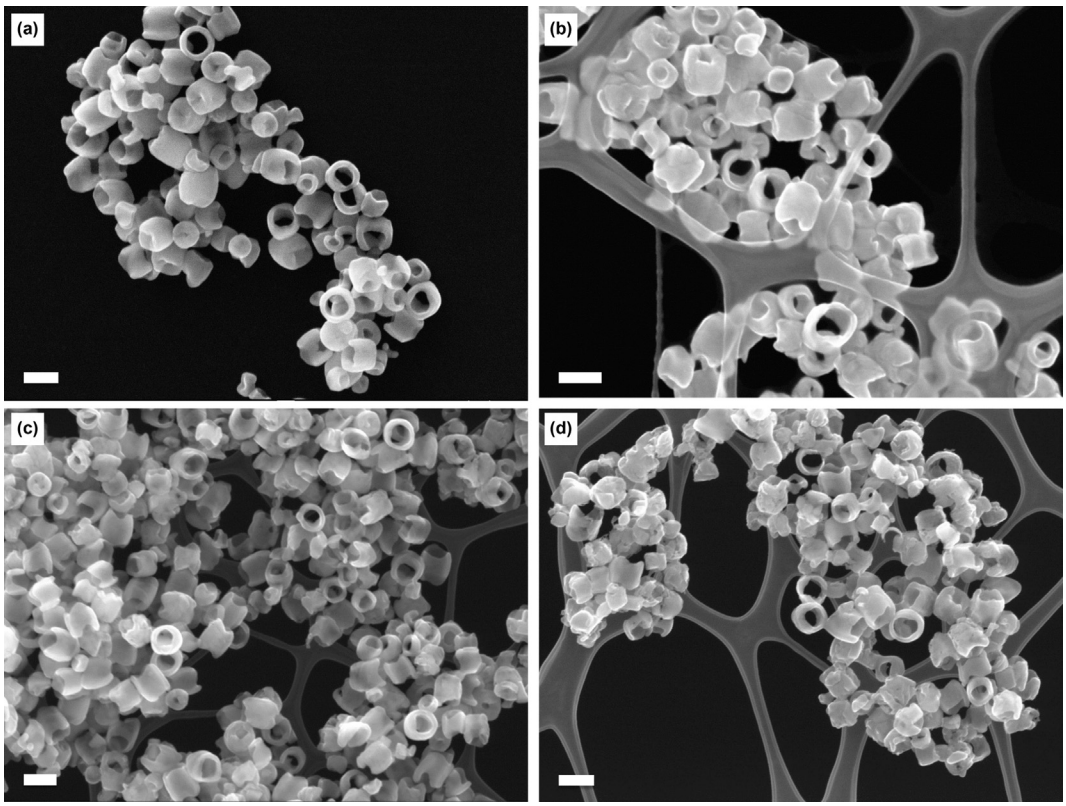

Fig. 2. SEM images of (a) hematite, (b) VIP5%, (c) VIP10% and (d) VIP70% nanoparticles, showing ring shape morphology, scale bars correspond to 200 nm.

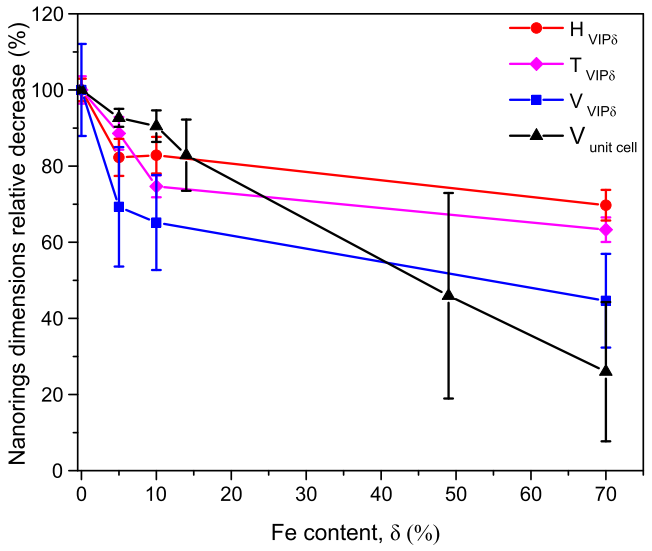

Fig. 3. Relative decrease of VIPδ nanoparticles dimensions after the reduction process: height (red), thickness (magenta), and volume (blue); and unit cell volume of VIPδ (black) as function of metallic iron content (δ). The δ = 0% represents hematite nanorings. (For interpretation of the references to color in this figure legend, the reader is referred to the web version of this article.)

images in (b), (c), and (d) are of VIP5%, VIP10%, and VIP70%, respectively. As can be observed from these FESEM images, the initial ring-like morphology was preserved, and the aspect ratio remained approximately the same even after significant reduction. However, after the reduction process, the dimensions of VIP δ decreased as a function of the iron content, as shown in Fig. 3 (the mean height is shown in red, the thickness defined as the difference between the external and internal diameters divided by two in magenta and, the volume of the nanoring in blue). These quantities were determinated from the ratio of the dimension of the samples before and after the reduction process. In other words, we used the following expression:

$$relative\ \ decrease = \frac{dimenssion_{after}}{dimenssion_{before}} * 100.$$

The volume of the nanorings decreased as the unit cell volume decreased (black line), because the unit cell volume of the metallic Fe is smaller than that of wustite, which, in turn, is smaller than that of magnetite/maghemite [48]. Therefore, increasing the amount of metallic Fe on the nanorings while ensuring that their morphology remains unchanged decreases the nanoring volume. Because the volumes of the unit cells of magnetite/maghemite, wustite, and metallic remained constant (see Fig. 1 (c)), it can be suggested that the nanorings were free of strain. In the VIPδ system with higher metallic iron concentration, this phase may be present on the surface of the nanotubes; in this case, the metallic iron would oxidates immediately after removing the samples from the oven with a controlled atmosphere. Therefore, the *ex-situ* XRD does not necessarily describe exactly the reduction dynamics. *In-situ* XRD experiments were performed at 400 °C in a 10% H_2/He gas flow to analyze the phases formed during the annealing under a controlled atmosphere avoiding possible oxidations and, therefore, more accurately describing the formation of metallic iron. The time evolution of the diffractograms over 120 min is shown in Fig. S4. These diffractograms were refined using the same method as that employed during the *ex-situ* measurements. This analysis made it possible to quantitatively analyze the time evolution of the contents of the different phases, as shown in Fig. 4(a). It can be seen that after 14 min of the reduction reaction, all of the hematite was transformed into maghemite/magnetite. As the reduction process continued, the maghemite/magnetite was continually converted into metallic iron. After 80 min of reduction,

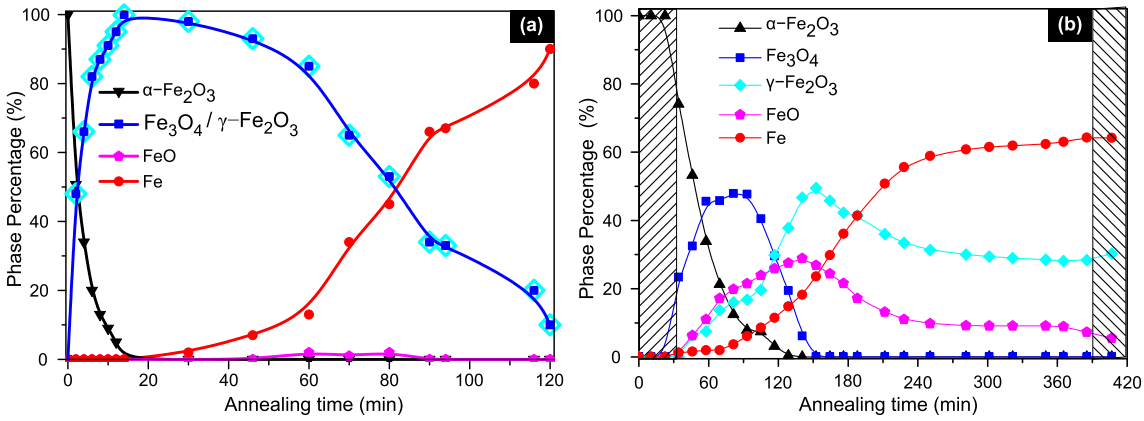

Fig. 4. Evolution of the phases percentage during *in situ* (a) XRD and (b) XANES experiments for hematite (black), magnetite (blue), maghemite (cyan), wustite (magenta), and metallic iron (red). Note that phases of magnetite and maghemite are shown together in same curve as *in situ* XRD measurements can not distinguish between these both phases; however they are shown separately in curves for *in situ* XANES measurements. Dashed regions indicate heating and cooling ramps. Error bars are on order of graph point symbol size. (For interpretation of the references to color in this figure legend, the reader is referred to the web version of this article.)

the metallic iron content of the nanoparticles was 50%. A small amount of wustite (1,5%) appeared as an intermediate phase as the reduction time was increased from 60 to 90 min. When the reduction time was increased further, the wustite was also transformed into metallic iron. Finally, after 120 min of reduction, the system was composed of 90% metallic iron and 10% maghemite/magnetite.

Therefore, the reduction dynamics under these conditions (*i.e.*, 400 °C and flow of 10% H_2/He) occurs in three steps, with the wustite appearing as an intermediate phase: $\alpha - Fe_2O_3 \rightarrow Fe_3O_4 \rightarrow FeO \rightarrow Fe$; where the oxidation state of iron changes as follows: $Fe^{3+} \rightarrow Fe^{3+} + Fe^{2+} \rightarrow Fe^{2+} \rightarrow Fe^0$.

The *in-situ* XANES measurements were performed at the Fe metal K-edge, at 400 °C in a 5% H_2/He flow to differentiate between maghemite and magnetite. Fig. S5 shows the time evolution of the normalized XANES spectra after 420 min of reduction. The phase quantification results are shown in Fig. 4 (b); the dashed regions indicate the heating and cooling ramp times. Note that during the heating stages, the hematite begins to transform into magnetite. The highest magnetite content (47.6%) was observed after 90 min, the remaining components being 17% maghemite, 21.5% wustite, and ~5.9% metallic iron. When the reduction time was increased to 150 min, the magnetite phase disappeared, and the maghemite phase fraction increased to 48.8%, with the remaining components being 26.7% wustite and 23.4% metallic iron. From this point onwards, the maghemite and wustite phases were transformed into metallic iron, with the final fractions being 64.7% metallic iron, 30.4% maghemite, and 5.4% wustite. On comparing the *in-situ* XRD and *in-situ* XANES measurements results, one can observe the following points: (i) the fraction of the wustite phase was higher during the XANES experiments, and (ii) the final content of metallic iron was 90% and 65%, respectively, during the XRD and XANES measurements. However, it is known that the hydrogen gas concentration plays a fundamental role during the reduction process, in that the lower the hydrogen concentration, the slower reduction dynamics will be [55]. Thus, considering the three reduction experiments conducted, namely, the *ex-situ* and *in-situ* XRD, and the *in-situ* XANES measurements, varying the reduction reaction parameters (such as the temperature, H_2 concentration, and reduction time) is an efficient strategy to control the final nanoring composition. Therefore, by adjusting these parameters, it is possible to readily tune the relative concentrations of metallic iron and its different oxides in the nanorings to optimize the magnetic properties. For instance, the shape of the hysteresis loop can be optimized for a given biomedical application in this manner.

From now on, the properties of the nanorings reduced with 10% H_2/Ar gas were explored further. All the experiments conducted were bulk sensitive. However, the core–shell structure resulted in the nanoparticles exhibiting unique surface properties. The results of XPS based surface analysis are given in Fig. 5, where (a) shows the XPS spectra and fitted enveloped for the *Fe2p* emission lines of the samples reduced for 60 (bottom), 120 (middle), and 240 min (top). The Fe 2p envelope is composed of Fe $2p_{1/2}$ and Fe $2p_{3/2}$ peaks, and the positions of these peaks agree with those reported for magnetite [54,56–59]. In addition, it was observed the absence of Fe $2p_{3/2}$ satellite peak, which is characteristic of magnetite [54]. The deconvolution of the Fe $2p_{1/2}$ peak indicated the presence of Fe^{2+} and Fe^{3+}; while the deconvolution of the Fe $2p_{3/2}$ peak indicated the presence of the metallic iron phase Fe^0. The atomic concentrations corresponding to these peaks were calculated and are listed in Table 1. It is known that Fe_3O_4 can be written as $FeO{\cdot}Fe_2O_3$, and that the Fe^{2+}:Fe^{3+} ratio must be 1:2 or 0.33:0.67 [33,54]. In the samples annealed for 60 and 240 min, the Fe^{2+}:Fe^{3+} ratio was 0.48 and 0.49, respectively, indicating the presence of stoichiometric magnetite on the surface. However, for the sample annealed for 120 min, this ratio was 0.66, indicating the presence of an excess amount of Fe^{2+}, which can be attributed to the presence of non-stoichiometric magnetite. We also compared the metallic iron content (δ) in the bulk (from the XRD analysis) and on the surface (from the XPS analysis) of the samples; Fig. 5 (b) shows that the metallic iron is located primarily within the VIPδ nanorings. In other words, the metallic iron is located in the core of the nanorings, resulting in a core–shell configuration for the VIPδ nanoparticles, whose surface is mainly composed of iron oxide.

The metallic iron of the samples increases the magnetic saturation as the magnetization value of metallic iron ($M_s^{Fe} = 220\ emu/g$) [60] is greater than those of magnetite and maghemite ($M_s^{Fe_3O_4} = 90\ emu/g$ [61,62] and $M_s^{\gamma-Fe_2O_3} = 60\ emu/g$ [63,64], respectively). In contrast to these phases, wustite is an antiferromagnetic iron oxide [65], and its magnetization saturation is $M_s^{FeO} = 0\ emu/g$. Therefore, if the phases contents of a sample are known, it is possible to estimate its magnetic saturation, which can be written as:

$$M_{s1} = \frac{\delta * M_s^{Fe} + \beta * M_s^{Fe_3O_4} + \rho * M_s^{FeO}}{100} emu/g \quad (1)$$

if the shell is composed of magnetite, or as:

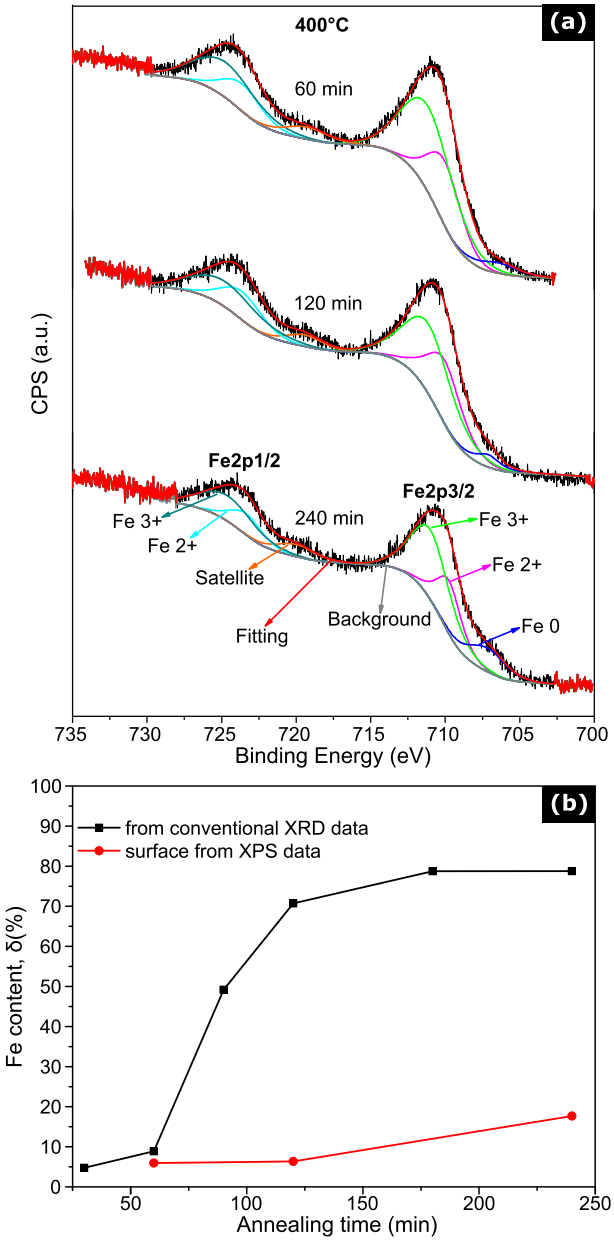

Fig. 5. (a) XPS spectra of nanorings annealed for 60 (top), 120 (middle), and 240 min (bottom). Fe 2p envelope peak was fitted for each sample, and Fe^{2+} (magenta), Fe^{3+} (green), and Fe^{0} (blue) were found on nanoparticles surfaces. (b) Comparison of Fe^{0} percentage in volume (XRD data) and on surface (XPS data) of samples as function of annealing time. Note that Fe^{0} percentage on the surface is smaller than that within sample, indicating that Fe^{0} was mostly present in sample interior, thus confirming the formation of core–shell configuration. Error bars are on order of graph point symbol size. (For interpretation of the references to color in this figure legend, the reader is referred to the web version of this article.)

$$M_{s2} = \frac{\delta * M_s^{Fe} + \beta * M_s^{\gamma-Fe_2O_3} + \rho * M_s^{FeO}}{100} emu/g \quad (2)$$

if the shell is composed of maghemite. In these equations, δ, β, and ρ are the phases content of metallic iron, magnetite/maghemite, and wustite, respectively, as determined from the *ex-situ* XRD data (Fig. 1 (b)). The magnetization of the selected samples is shown in Fig. 6(a) as function of the magnetic field at room temperature; the magnetization increases with increasing metallic iron content (δ). The saturation magnetization of the core–shell particles as a

Table 1
Deconvolution of Fe 2p peaks and corresponding atomic concentrations.

Annealing time (min)	Peak	Peak composition	Atomic concentration (%)	Fe^{+2}: Fe^{+3}
60	$Fe2p_{3/2}$	Fe^{2+}	19.84	0.48
		Fe^{3+}	40.96	
		Fe^{0}	6.45	
	$Fe2p_{1/2}$	Fe^{2+}	9.96	0.48
		Fe^{3+}	20.57	
120	$Fe2p_{3/2}$	Fe^{2+}	24.25	0.66
		Fe^{3+}	36.86	
		Fe^{0}	5.66	
	$Fe2p_{1/2}$	Fe^{2+}	12.17	0.66
		Fe^{3+}	18.51	
240	$Fe2p_{3/2}$	Fe^{2+}	18.09	0.49
		Fe^{3+}	36.60	
		Fe^{0}	19.12	
	$Fe2p_{1/2}$	Fe^{2+}	9.08	0.49
		Fe^{3+}	18.38	

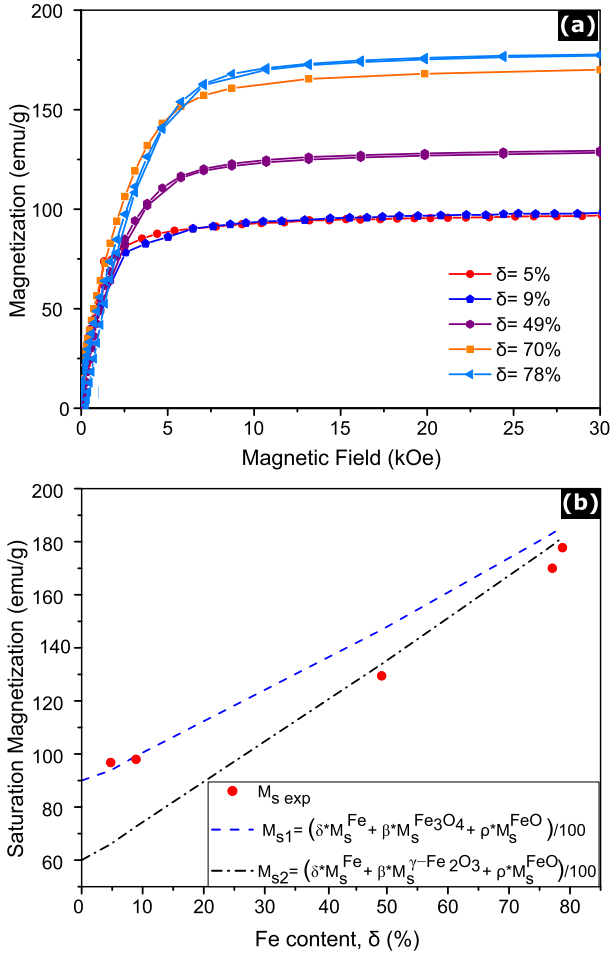

Fig. 6. (a) Magnetization as function of magnetic field at room temperature for selected samples with different metallic iron contents (δ); (b) magnetization saturation at room temperature as function of metallic iron content (δ) as determined through magnetic measurement (red points), theoretical magnetization saturation M_{s1} and M_{s2} are represented by dashed blue and black lines, respectively. Magnetization saturation increases with increasing metallic iron content. Error bars are on order of graph point symbol size. (For interpretation of the references to color in this figure legend, the reader is referred to the web version of this article.)

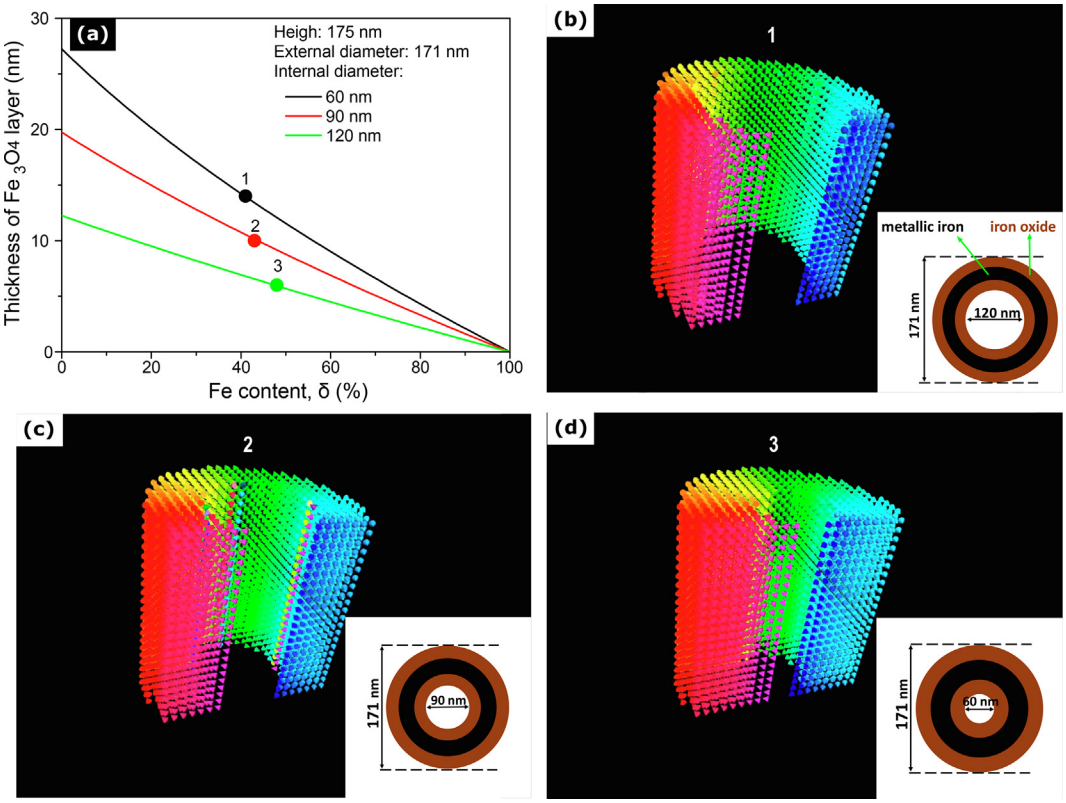

Fig. 7. (a) Simulated thickness of magnetite layer as function of metallic iron content for nanorings with H = 175 nm, D = 171 nm, and three different internal diameters (d): 120 (90 + 30) nm (green line); 90 nm (red line); and 60 (90–30) nm (black line). Points (1), (2), and (3) represent selected simulated nanorings illustrated in (b) for δ = 41%, (c) δ = 43%, and (d) δ = 48%, respectively. Note that the ground state is vortex configuration. (For interpretation of the references to color in this figure legend, the reader is referred to the web version of this article.)

function of the metallic iron content (δ) is shown in Fig. 6 (b); the dashed blue and black lines represent the calculated magnetization M_{s1} and M_{s2}, respectively. Note that for low metallic iron contents (δ), the experimental saturation is close to M_{s1}, indicating that the shell is composed of magnetite, in keeping with the XPS and *in-situ* XANES results. For intermediate and high metallic iron contents (δ), the experimental saturation is close to M_{s2}, indicating that maghemite is the main component of the shell. These results agree with the *in-situ* XANES results, which showed that for metallic iron contents of 30% and higher, the iron oxide is maghemite and not magnetite.

It is well known that magnetite nanoring exhibit a magnetic vortex arrangement as the ground state [32]. However, this is not the case for the VIPδ system. Thus, to determinate whether this system also exhibits vortex arrangement, we performed systematic micromagnetic analyses using the MuMax3 package. For these simulations, we used a nanoring composed of a metallic iron core covered by a magnetite shell. The dimensions (D, d, and H) of the nanorings used for the simulations were two deviations from those measured by FESEM. In other words, all possible combinations of $\langle D \rangle = (170 \pm 30)$ nm, $\langle d \rangle = (90 \pm 30)$ nm and $\langle H \rangle = (175 \pm 35)$ nm were used. To mimic the metallic Fe shell corresponding to a given Fe concentration, we considered an iron oxide layer with a constant thickness and assumed that it covered the entire nanoring. The relationship between the Fe layer thickness and the Fe concentration (δ) was determined geometrically using the ratio of the shell and core volumes, for each dimension. The Fe concentration was varied (as was the Fe thickness) from zero (pure magnetite nanoring) to 100%. A specific curve for the Fe thickness as function of the Fe concentration was obtained for a given set of dimensions (D, d, and H), as shown in Fig. 7 (a). To determine the ground state of each nanoring, simulations were performed using three different initial magnetic configurations, namely, a magnetic vortex and a uniform magnetization point parallel and perpendicular to the height axis of the nanoring (saturated magnetization condition). Then, the magnetic configuration was allowed to relax to minimize the total energy until it reached a final magnetic configuration, corresponding to the local minimum energy. The final magnetic configuration was considered the ground state of the specific nanoring, which corresponded to the final total energy lower value. Fig. 7 shows that the ground state corresponds to the vortex configuration in the case of the nanorings with an internal diameter of (b) 120, (c) 90, and (d) 60 nm. The magnetic vortex configuration was the ground state for every simulated nanoring, irrespective of the nanoring dimensions and metallic iron concentration. For this reason, we believe that all samples exhibited a vortex configuration, irrespective of their metallic iron concentration.

3.3. Biological tests

To verify the cytotoxic dose of VIP78% (*i.e.*, the sample with a metallic iron content of 78%), we performed the MTT assay using two different cell lines, namely, HEK293 (epithelial cells from human kidney embryo) and SAOS2 (human osteosarcoma cell line) (see Fig. 8 (a) and (b), respectively). The results showed that, in the case of HEK293 cells, the maximum non-cytotoxic dose was 100 μg/mL. In contrast, the SAOS2 cells showed greater resistance to the VIP78%, exhibiting no signs of cytotoxicity even after exposure to the nanorings at a concentration of 500 μg/mL. Since MTT is a colorimetric assay, to verify whether the color of the iron particles interfered with the assay, we tested the cells after exposure at a concentration of 100 μg/mL using the live/dead assay. This

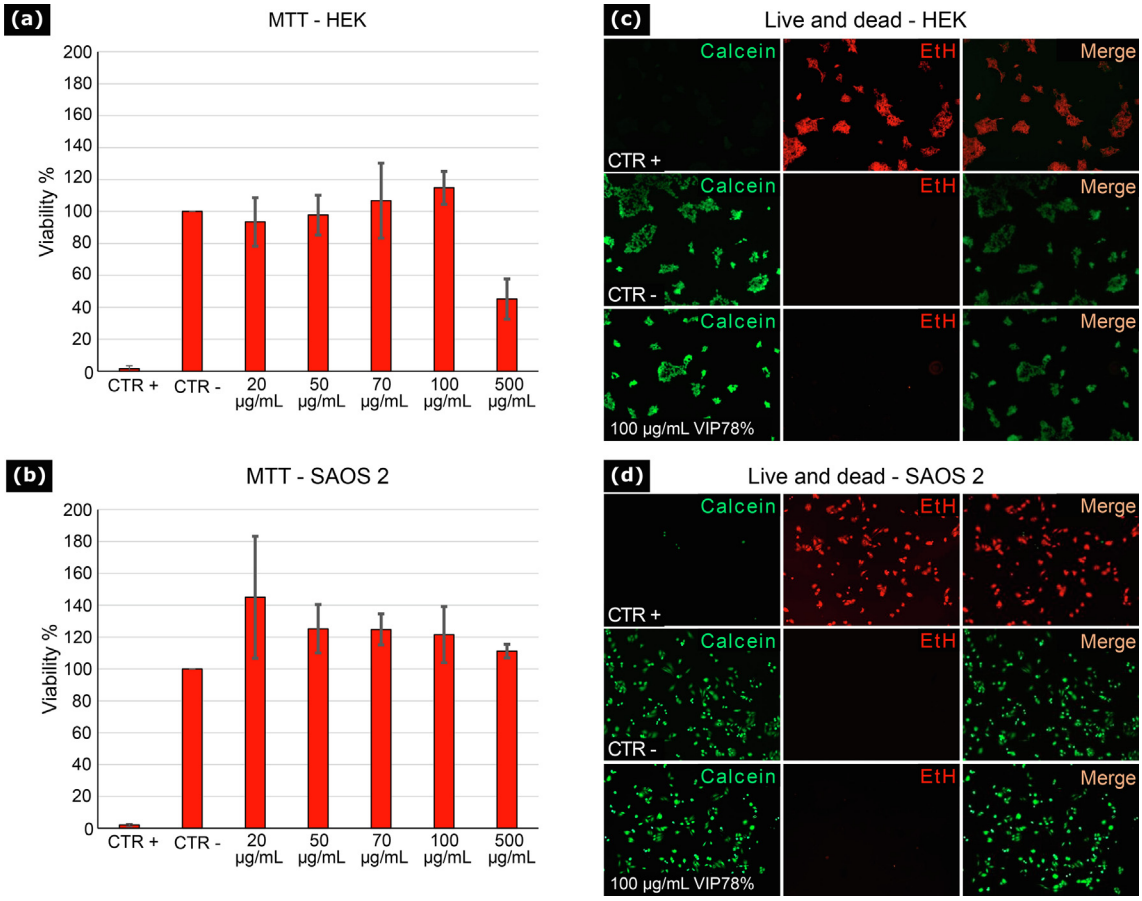

Fig. 8. Viability of (a) HEK and (b) SAOS2 cells determined by MTT assay after 24 h of exposure to VIP78%; (c), (d) fluorescence microscopy images of live/dead assay after 24 h of exposure to 100 µg/mL of VIP78% for HEK and SAOS2 cells line, respectively. Live cells are shown in green (calcein positive), while dead cells are shown in red (ethidium positive). Merged images show overlapping live and dead cells. (For interpretation of the references to color in this figure legend, the reader is referred to the web version of this article.)

assay is a two-color assay based on integrity of the plasma membrane and esterase activity and is used to determine cell viability. Since it is a fluorescent assay, it eliminates the interference observed from the color of the material used during the calorimetric assay as MTT. In addition, this test can discriminate a single cell event based on simultaneous cell staining using the intracellular esterase activity, generating green-fluorescent calcein-AM (AM, acetoxymethyl) to indicate live cells and fluorescent ethidium homodimer-1 which owing to the loss of the plasma membrane integrity, can reach and stain the DNA (deoxyribonucleic acid) in red, indicating dead cells. Fig. 8(c) and (d) show fluorescence microscopy images of the HEK and SAOS2 cells line, respectively. Live cells stained green (Calcein positive) and dead cells stained red (Ethidium positive, EtH). However, significant cell death was not observed in the case of either cells lines, corroborating the MTT assay results. Furthermore, a concentration of 100 µg/mL was determined to the maximum non–cytotoxic dose of VIP78% concentration for both cell types. The high biocompatibility of VIP78% is attributable to the presence of magnetite/maghemite on the nanoparticle surfaces; since this iron oxide is well-known biocompatible [66] and can isolate the highly reactive metallic iron. It is important to highlight the fact that the VIP78% nanoparticles had the finest surface layer of iron oxide. Therefore, it is expected that the other VIPδ samples (*i.e.*, those with $\delta \leq 78\%$) would also exhibit biocompatibility.

4. Conclusions

In summary, through a combination of hydrothermal synthesis and controlled reduction processes, we fabricated VIPδ nanorings with a core–shell structure composed of metallic Fe (core) and iron oxide (shell). Thus, the nanorings exhibit the biocompatibility of de iron oxide combined with the high magnetic saturation of metallic iron. The reduction process was studied in detail using both *ex-situ* and *in-situ* X-ray techniques. It was found that controlling the reduction time, as well as the hydrogen concentration, is crucial for optimizing the metallic iron content and hence the magnetic parameters. For short reduction times and weak hydrogen reduction conditions, the metallic iron content was low, and therefore the magnetic properties of iron oxide dominated the resulting system. In contrast, for longer reduction times and strong hydrogen reduction conditions, the metallic iron content was higher, and so were the magnetic saturation values. Micro-magnetic simulations provided information regarding the expected vortex-type magnetic behavior based on the ring-like morphology of the nanoparticles. In addition, the results of cytotoxicity tests performed using VIP78% on HEK293 and SAOS2 cell types confirmed that the cells showed high resistance to the nanoparticle. Thus, the nanoparticles exhibited high biocompatibility and did not result in significant cell death despite the presence of the metallic iron core. These properties make VIPδ a versatile system for use in

various bioapplications such as drug delivery, magnetic hyperthermia, magnetic separations, and magnetic resonance imaging. Nevertheless, the hydrothermal extended reaction process needs to be overcome, and the effects of large-scale of the system for future commercial production needs investigation. Several challenges must be addressed; thus, investigations of the crystalline structure at the nanoscale using Synchrotron Radiation source; the colloidal stability and the uptake of VIPδ by cells using *in situ* transmission electron microscopy; *in vitro* magnetic hyperthermia, and drug delivery. All these points are part of ongoing studies to validate the conclusions obtained from the present study.

CRediT authorship contribution statement

Bianca M. Galeano-Villar: Methodology, Validation, Formal analysis, Investigation, Writing – original draft, Visualization. **Richard J. Caraballo-Vivas:** Methodology, Validation, Formal analysis, Investigation, Writing – original draft, Visualization. **Evelyn C. S. Santos:** Investigation, Visualization, Writing – original draft. **Raimundo C. Rabelo-Neto:** Investigation. **Sara Gemini-Piperni:** Investigation. **Priscilla V. Finotelli:** Conceptualization, Writing – review & editing. **Noemi R. Checca:** Investigation. **Carlos S.B. Dias:** Investigation, Writing – review & editing. **Flávio Garcia:** Conceptualization, Writing – review & editing, Supervision, Project administration.

Declaration of Competing Interest

The authors declare that they have no known competing financial interests or personal relationships that could have appeared to influence the work reported in this paper.

Acknowledgements

We acknowledge the brazilian funders FAPERJ, CAPES, and CNPq for financial support. RJCV is thankful for Grant No. E-26/202.319/2018 from FAPERJ. FG is grateful to CAPES for Grant No. 308352/2019-0. Thank the LNLS for the assigned schedule at XRD-1 (20160336) and DXAS (20180513) beamlines to perform the *in-situ* XRD and XANES, respectively. Gratefulness to CBPF Laboratories for the schedule: X-ray Laboratory, Laboratory of Surface and Nanostructures, Interinstitutional Magnetic measurement and Transport Laboratory and, LABNANO.

Appendix A. Supplementary material

Supplementary data to this article can be found online at https://doi.org/10.1016/j.matdes.2021.110303.

References

[1] K.S. Kim, J. Kim, J.Y. Lee, S. Matsuda, S. Hideshima, Y. Mori, T. Osaka, K. Na, Stimuli-responsive magnetic nanoparticles for tumor-targeted bimodal imaging and photodynamic/hyperthermia combination therapy, Nanoscale 8 (22) (2016) 11625–11634, https://doi.org/10.1039/C6NR02273A.
[2] C.M. Ellis, J. Pellico, J.J. Davis, Magnetic nanoparticles supporting bio-responsive T1/T2 magnetic resonance imaging, Materials (Basel) 12 (2019) 1–13, https://doi.org/10.3390/ma1224096.
[3] E.C.S. Santos, A. Watanabe, M.D. Vargas, M.N. Tanaka, F. Garcia, C.M. Ronconi, AMF-responsive doxorubicin loaded b-cyclodextrin-decorated superparamagnetic nanoparticles, New J. Chem. 42 (2018) 671–680, https://doi.org/10.1039/C7NJ02860A.
[4] A. Hervault, A.E. Dunn, M. Lim, C. Boyer, D. Mott, S. Maenosono, N.T.K. Thanh, Doxorubicin loaded dual pH- and thermo-responsive magnetic nanocarrier for combined magnetic hyperthermia and targeted controlled drug delivery applications, Nanoscale 8 (24) (2016) 12152–12161, https://doi.org/10.1039/C5NR07773G.
[5] N.V.S. Vallabani, S. Singh, A.S. Karakoti, Magnetic nanoparticles: current trends and future aspects in diagnostics and nanomedicine, Curr. Drug Metab. 20 (6) (2019) 457–472, https://doi.org/10.2174/1389200220666181122124458.
[6] T. Marín, P. Montoya, O. Arnache, R. Pinal, J. Calderón, Development of magnetite nanoparticles/gelatin composite films for triggering drug release by an external magnetic field, Mater. Des. 152 (2018) 78–87, https://doi.org/10.1016/J.MATDES.2018.04.073.
[7] A.H. Haghighi, M.T. Khorasani, Z. Faghih, F. Farjadian, Effects of different quantities of antibody conjugated with magnetic nanoparticles on cell separation efficiency, Heliyon 6 (4) (2020) e03677, https://doi.org/10.1016/j.heliyon.2020.e03677.
[8] A. Saei, S. Asfia, H. Kouchakzadeh, M. Rahmandoust, Antibody-modified magnetic nanoparticles as specific high-efficient cell-separation agents, J. Biomed. Mater. Res. Part B Appl. Biomater. 108 (6) (2020) 2633–2642, https://doi.org/10.1002/jbm.b.34595.
[9] T.S. Fernandes, E.C.S. Santos, V.G.C. Madriaga, I.A.A. Bessa, V. Nascimento, F. Garcia, C.M. Ronconi, A self-assembled AMF-responsive nanoplatform based on pillar[5]arene and superparamagnetic nanoparticles for controlled release of doxorubicin, J. Braz. Chem. Soc. 30 (2019) 2452–2463. https://doi.org/10.21577/0103-5053.20190164.
[10] C.A. Quinto, P. Mohindra, S. Tong, G. Bao, Multifunctional superparamagnetic iron oxide nanoparticles for combined chemotherapy and hyperthermia cancer treatment, Nanoscale 7 (29) (2015) 12728–12736.
[11] A. Hervault, N.T.K. Thanh, Magnetic nanoparticle-based therapeutic agents for thermo-chemotherapy treatment of cancer, Nanoscale 6 (20) (2014) 11553–11573, https://doi.org/10.1039/C4NR03482A.
[12] M.E.F. Brollo, J.M. Orozco-henao, R. López-ruiz, D. Muraca, C.S.B. Dias, K.R. Pirota, M. Knobel, Magnetic hyperthermia in brick-like Ag @ Fe 3 O 4 core – shell nanoparticles, J. Magn. Magn. Mater. 397 (2016) 20–27, https://doi.org/10.1016/j.jmmm.2015.08.081.
[13] S. Mornet, S. Vasseur, F. Grasset, P. Veverka, G. Goglio, A. Demourgues, J. Portier, E. Pollert, E. Duguet, Magnetic nanoparticle design for medical applications, Prog. Solid State Chem. 34 (2-4) (2006) 237–247.
[14] M. Bañobre-López, A. Teijeiro, J. Rivas, Magnetic nanoparticle-based hyperthermia for cancer treatment, Reports Pract. Oncol. Radiother. 18 (6) (2013) 397–400.
[15] E.C.S. Santos, J.A. Cunha, M.G. Martins, B.M. Galeano-Villar, R.J. Caraballo-Vivas, P.B. Leite, A.L. Rossi, F. Garcia, P.V. Finotelli, H.C. Ferraz, Curcuminoids-conjugated multicore magnetic nanoparticles: design and characterization of a potential theranostic nanoplatform, J. Alloys Compd. 879 (2021) 160448, https://doi.org/10.1016/j.jallcom.2021.160448.
[16] S. Laurent, S. Dutz, U.O. Häfeli, M. Mahmoudi, Magnetic fluid hyperthermia: Focus on superparamagnetic iron oxide nanoparticles, Adv. Colloid Interface Sci. 166 (1-2) (2011) 8–23, https://doi.org/10.1016/j.cis.2011.04.003.
[17] Z. Nemati, J. Alonso, H. Khurshid, M.H. Phan, H. Srikanth, Core/shell iron/iron oxide nanoparticles: are they promising for magnetic hyperthermia?, RSC Adv 6 (45) (2016) 38697–38702, https://doi.org/10.1039/C6RA05064F.
[18] I. Sharifi, H. Shokrollahi, S. Amiri, Ferrite-based magnetic nanofluids used in hyperthermia applications, J. Magn. Magn. Mater. 324 (6) (2012) 903–915.
[19] S.I. El-Dek, M.A. Ali, S.M. El-Zanaty, S.E. Ahmed, Comparative investigations on ferrite nanocomposites for magnetic hyperthermia applications, J. Magn. Magn. Mater. 458 (2018) 147–155.
[20] L. Xing, G.H. Ten Brink, B. Chen, F.P. Schmidt, G. Haberfehlner, F. Hofer, B.J. Kooi, G. Palasantzas, Synthesis and morphology of iron-iron oxide core-shell nanoparticles produced by high pressure gas condensation, Nanotechnology 27 (2016) 1–10, https://doi.org/10.1088/0957-4484/27/21/215703.
[21] H. Khurshid, V. Tzitzios, W. Li, C.G. Hadjipanayis, G.C. Hadjipanayis, Size and composition control of core-shell structured iron/iron-oxide nanoparticles, J. Appl. Phys. 107 (9) (2010) 09A333, https://doi.org/10.1063/1.3368720.
[22] A. Ahmad, H. Bae, I. Rhee, Cube-shaped cetyltrimethyl ammonium bromide-coated nickel ferrite nanoparticles for hyperthermia applications, J. Korean Phys. Soc. 73 (1) (2018) 125–129.
[23] V.K. Sharma, A. Alipour, Z. Soran-Erdem, Z.G. Aykut, H.V. Demir, Highly monodisperse low-magnetization magnetite nanocubes as simultaneous T1–T2 MRI contrast agents, Nanoscale 7 (23) (2015) 10519–10526.
[24] A. Nikitin, M. Khramtsov, A. Garanina, P. Mogilnikov, N. Sviridenkova, I. Shchetinin, A. Savchenko, M. Abakumov, A. Majouga, Synthesis of iron oxide nanorods for enhanced magnetic hyperthermia, J. Magn. Magn. Mater. 469 (2019) 443–449.
[25] Y.P. Ivanov, A. Alfadhel, M. Alnassar, J.E. Perez, M. Vazquez, A. Chuvilin, J. Kosel, Tunable magnetic nanowires for biomedical and harsh environment applications, Sci. Rep. 6 (2016) 1–10, https://doi.org/10.1038/srep24189.
[26] G. Kandasamy, S. Khan, J. Giri, S. Bose, N.S. Veerapu, D. Maity, One-pot synthesis of hydrophilic flower-shaped iron oxide nanoclusters (IONCs) based ferrofluids for magnetic fluid hyperthermia applications, J. Mol. Liq. 275 (2019) 699–712.
[27] S. Del Sol-Fernández, Y. Portilla-Tundidor, L. Gutiérrez, O.F. Odio, E. Reguera, D. F. Barber, M.P. Morales, Flower-like Mn-doped magnetic nanoparticles functionalized with αvβ3-integrin-ligand to efficiently induce intracellular heat after alternating magnetic field exposition, triggering glioma cell death, ACS Appl. Mater. Interfaces 11 (30) (2019) 26648–26663, https://doi.org/10.1021/acsami.9b0831810.1021/acsami.9b08318.s001.
[28] E.C. Abenojar, S. Wickramasinghe, J. Bas-Concepcion, A.C.S. Samia, Structural effects on the magnetic hyperthermia properties of iron oxide nanoparticles, Prog. Nat. Sci. Mater. Int. 26 (5) (2016) 440–448.
[29] J. Mohapatra, M. Xing, J. Beatty, J. Elkins, T. Seda, S.R. Mishra, J.P. Liu, Enhancing the magnetic and inductive heating properties of Fe3O4 nanoparticles via morphology control, Nanotechnology 31 (2020), https://doi.org/10.1016/j.jhazmat.2007.06.077.

[30] R. Das, J.A. Masa, V. Kalappattil, Z. Nemati, I. Rodrigo, E. Garaio, J.Á. García, M.-H. Phan, H. Srikanth, L. Fuente, Iron oxide nanorings and nanotubes for magnetic hyperthermia: the problem of intraparticle, Interactions (2021), https://doi.org/10.3390/nano11061380.
[31] C.S.B. Dias, T.D.M. Hanchuk, H. Wender, W.T. Shigeyosi, J. Kobarg, A.L. Rossi, M. N. Tanaka, M.B. Cardoso, F. Garcia, Shape tailored magnetic nanorings for intracellular hyperthermia cancer therapy, Sci. Rep. 7 (2017) 14843.
[32] C.-J. Jia, L.-D. Sun, F. Luo, X.-D. Han, L.J. Heyderman, Z.-G. Yan, C.-H. Yan, K. Zheng, Z.e. Zhang, M. Takano, N. Hayashi, M. Eltschka, M. Kläui, U. Rüdiger, T. Kasama, L. Cervera-Gontard, R.E. Dunin-Borkowski, G. Tzvetkov, J. Raabe, et al., Large-scale synthesis of single-crystalline iron oxide magnetic nanorings, J. Am. Chem. Soc. 130 (50) (2008) 16968–16977.
[33] G. Niraula, J.A.H. Coaquira, F.H. Aragon, B.M. Galeano Villar, A. Mello, F. Garcia, D. Muraca, G. Zoppellaro, J.M. Vargas, S.K. Sharma, Tuning the shape, size, phase composition and stoichiometry of iron oxide nanoparticles: the role of phosphate anions, J. Alloys Compd. 856 (2021) 156940, https://doi.org/10.1016/j.jallcom.2020.156940.
[34] G. Niraula, J.A.H. Coaquira, F.H. Aragon, A.F. Bakuzis, B.M.G. Villar, F. Garcia, D. Muraca, G. Zoppellaro, A.I. Ayesh, S.K. Sharma, S. Luis, C. Republic, Stoichiometry and orientation/shape mediated switching field enhancement on heating properties of Fe 3 O 4 circular nanodiscs, Phys. Rev. Appl 15 (2021) 1–14, https://doi.org/10.1103/PhysRevApplied.0.XXXXXX.
[35] D. Gregurec, A.W. Senko, A. Chuvilin, P.D. Reddy, A. Sankararaman, D. Rosenfeld, P.-H. Chiang, F. Garcia, I. Tafel, G. Varnavides, E. Ciocan, P. Anikeeva, Magnetic vortex nanodiscs enable remote magnetomechanical neural stimulation, ACS Nano 14 (7) (2020) 8036–8045, https://doi.org/10.1021/acsnano.0c0056210.1021/acsnano.0c00562.s00110.1021/acsnano.0c00562.s00210.1021/acsnano.0c00562.s00310.1021/acsnano.0c00562.s004.
[36] X.-L. Liu, Y. Yang, J.-P. Wu, Y.-F. Zhang, H.-M. Fan, J. Ding, Novel magnetic vortex nanorings/nanodiscs: synthesis and theranostic applications, Chinese Phys. B. 24 (12) (2015) 127505, https://doi.org/10.1088/1674-1056/24/12/127505.
[37] G. Niraula, J.A.H. Coaquira, G. Zoppellaro, B.M.G. Villar, F. Garcia, A.F. Bakuzis, J. P.F. Longo, M.C. Rodrigues, D. Muraca, A.I. Ayesh, F.S.M. Sinfrônio, A.S. de Menezes, G.F. Goya, S.K. Sharma, Engineering shape anisotropy of Fe 3 O 4-γ-Fe 2 O 3 hollow nanoparticles for magnetic hyperthermia, ACS Appl. Nano Mater. 4 (3) (2021) 3148–3158, https://doi.org/10.1021/acsanm.1c0031110.1021/acsanm.1c00311.s001.
[38] A.P. Guimarães, Principles of Nanomagnetism, second ed., Springer, 2017.
[39] D.F. Gutierrez-Guzman, L.I. Lizardi, J.A. Otálora, P. Landeros, Hyperthermia in low aspect-ratio magnetic nanotubes for biomedical applications, Appl. Phys. Lett. 110 (13) (2017) 133702, https://doi.org/10.1063/1.4979165.
[40] M. Marciello, V. Connord, S. Veintemillas-Verdaguer, M.A. Vergés, J. Carrey, M. Respaud, C.J. Serna, M.P. Morales, Large scale production of biocompatible magnetite nanocrystals with high saturation magnetization values through green aqueous synthesis, J. Mater. Chem. B 1 (2013) 5995–6004, https://doi.org/10.1039/c3tb20949k.
[41] R. Das, C. Witanachchi, Z. Nemati, V. Kalappattil, I. Rodrigo, J.Á. García, E. Garaio, J. Alonso, V.D. Lam, A.T. Le, M.H. Phan, H. Srikanth, Magnetic vortex and hyperthermia suppression in multigrain iron oxide nanorings, Appl. Sci. 10 (2020) 1–11, https://doi.org/10.3390/app10030787.
[42] H.-M. Fan, J.-B. Yi, Y.i. Yang, K.-W. Kho, H.-R. Tan, Z.-X. Shen, J. Ding, X.-W. Sun, M.C. Olivo, Y.-P. Feng, Single-crystalline MFe2O4 nanotubes/nanorings synthesized by thermal transformation process for biological applications, ACS Nano 3 (9) (2009) 2798–2808.
[43] X. Liu, J. Zheng, W. Sun, X. Zhao, Y. Li, N. Gong, Y. Wang, X. Ma, T. Zhang, L.-Y. Zhao, Y. Hou, Z. Wu, Y. Du, H. Fan, J. Tian, X.-J. Liang, Ferrimagnetic vortex nanoring-mediated mild magnetic hyperthermia imparts potent immunological effect for treating cancer metastasis, ACS Nano 13 (8) (2019) 8811–8825, https://doi.org/10.1021/acsnano.9b01979.
[44] H.-M. Fan, M. Olivo, B. Shuter, J.-B. Yi, R. Bhuvaneswari, H.-R. Tan, G.-C. Xing, C.-T. Ng, L. Liu, S.S. Lucky, B.-H. Bay, J. Ding, Quantum dot capped magnetite nanorings as high performance nanoprobe for multiphoton fluorescence and magnetic resonance imaging, J. Am. Chem. Soc. 132 (42) (2010) 14803–14811, https://doi.org/10.1021/ja103738t.
[45] C.S.B. Dias, F. Garcia, I.O. Mazali, M.B. Cardoso, J.M. de S. e Silva, Direct route for preparing multi-oxide inorganic nanocomposites of nanoparticles-decorated nanotubes, J. Alloys Compd. 774 (2019) 1133–1139.
[46] J. Rodriguez-Carvajal, FULLPROF: a program for Rietveld refinement and pattern matching analysis, in: Satell. Meet. Powder Diffr. XV Congr. IUCr, 1990.
[47] A.S. Kamzin, A.A. Valiullin, H. Khurshid, Z. Nemati, H. Srikanth, M.H. Phan, Mössbauer studies of core-shell FeO/Fe 3 O 4 nanoparticles, Phys. Solid State 60 (2) (2018) 382–389.
[48] O. Crisan, A.D. Crisan, Phase transformation and exchange bias effects in mechanically alloyed Fe/magnetite powders, J. Alloys Compd. 509 (23) (2011) 6522–6527.
[49] W.B.F. Jalil, A. Pentón-Madrigal, A. Mello, F.A. Carneiro, R.M. Soares, L.S. Baptista, J.P. Sinnecker, L.A.S. de Oliveira, Low toxicity superparamagnetic magnetite nanoparticles: one-pot facile green synthesis for biological applications, Mater. Sci. Eng., C 78 (2017) 457–466.
[50] J.C. Cezar, N.M. Souza-Neto, C. Piamonteze, E. Tamura, F. Garcia, E.J. Carvalho, R.T. Neueschwander, A.Y. Ramos, H.C.N. Tolentino, A. Caneiro, N.E. Massa, M.J. Martinez-Lope, J.A. Alonso, J.-P. Itié, Energy-dispersive X-ray absorption spectroscopy at LNLS: investigation on strongly correlated metal oxides, J. Synchrotron Radiat. 17 (1) (2010) 93–102, https://doi.org/10.1107/S0909049509041119.
[51] A.M.G. Carvalho, R.S. Nunes, A.A. Coelho, X-ray powder diffraction of high-absorption materials at the XRD1 beamline off the best conditions: Application to (Gd, Nd) 5 Si 4 compounds, Powder Diffr. 32 (2017) 10–14.
[52] J.F. De Carvalho, S.N. De Medeiros, M.A. Morales, A.L. Dantas, A.S. Carriço, Synthesis of magnetite nanoparticles by high energy ball milling, Appl. Surf. Sci. 275 (2013) 84–87, https://doi.org/10.1016/j.apsusc.2013.01.118.
[53] D. Fiorani, A.M. Testa, F. Lucari, F. D'Orazio, H. Romero, Magnetic properties of maghemite nanoparticle systems: surface anisotropy and interparticle interaction effects, Phys. B Condens. Matter. 320 (1-4) (2002) 122–126, https://doi.org/10.1016/S0921-4526(02)00659-2.
[54] T. Yamashita, P. Hayes, Analysis of XPS spectra of Fe 2+ and Fe 3+ ions in oxide materials, Appl. Surf. Sci. 254 (8) (2008) 2441–2449, https://doi.org/10.1016/j.apsusc.2007.09.063.
[55] J. Zieliński, I. Zglinicka, L. Znak, Z. Kaszkur, Reduction of Fe2O3 with hydrogen, Appl. Catal. A Gen. 381 (1-2) (2010) 191–196.
[56] M. Oku, K. Hirokawa, X-ray photoelectron spectroscopy of Co3O4, Fe3O4, Mn3O4, and related compounds, J. Electron Spectros. Relat. Phenomena. 8 (5) (1976) 475–481, https://doi.org/10.1016/0368-2048(76)80034-5.
[57] D.D. Hawn, B.M. DeKoven, Deconvolution as a correction for photoelectron inelastic energy losses in the core level XPS spectra of iron oxides, Surf. Interface Anal. 10 (2-3) (1987) 63–74, https://doi.org/10.1002/sia.740100203.
[58] P. Marcus, J.M. Grimal, The anodic dissolution and passivation of NiCrFe alloys studied by ESCA, Corros. Sci. 33 (5) (1992) 805–814, https://doi.org/10.1016/0010-938X(92)90113-H.
[59] B.J. Tan, K.J. Klabunde, P.M.A. Sherwood, X-ray photoelectron spectroscopy studies of solvated metal atom dispersed catalysts. Monometallic iron and bimetallic iron-cobalt particles on alumina, Chem. Mater. 2 (2) (1990) 186–191, https://doi.org/10.1021/cm00008a021.
[60] H. Khurshid, C.G. Hadjipanayis, H. Chen, W. Li, H. Mao, R. Machaidze, V. Tzitzios, G.C. Hadjipanayis, Core/shell structured iron/iron-oxide nanoparticles as excellent MRI contrast enhancement agents, J. Magn. Magn. Mater. 331 (2013) 17–20.
[61] H. Aali, S. Mollazadeh, J.V. Khaki, Single-phase magnetite with high saturation magnetization synthesized via modified solution combustion synthesis procedure, Ceram. Int. 44 (16) (2018) 20267–20274.
[62] S.J. Kemp, R.M. Ferguson, A.P. Khandhar, K.M. Krishnan, Monodisperse magnetite nanoparticles with nearly ideal saturation magnetization, RSC Adv. 6 (81) (2016) 77452–77464.
[63] C. Goss, Saturation magnetisation, coercivity and lattice parameter changes in the system Fe304-yFe2O3, and their relationship to structure, Phys. Chem. Miner. 16 (1988) 164–171.
[64] F. Zeb, K. Nadeem, S.K.A. Shah, M. Kamran, I.H. Gul, L. Ali, Surface spins disorder in uncoated and SiO2 coated maghemite nanoparticles, J. Magn. Magn. Mater. 429 (2017) 270–275, https://doi.org/10.1016/j.jmmm.2017.01.040.
[65] G.C. Papaefthymiou, Nanoparticle magnetism, Nano Today 4 (5) (2009) 438–447, https://doi.org/10.1016/j.nantod.2009.08.006.
[66] A.K. Gupta, M. Gupta, Synthesis and surface engineering of iron oxide nanoparticles for biomedical applications, Biomaterials 26 (18) (2005) 3995–4021, https://doi.org/10.1016/j.biomaterials.2004.10.012.